Ab initio investigation of the magnetic and ferroelectric properties of BaCuF$_4$ under hydrostatic pressure

David Vincent● and Xavier Rocquefelte●[*]

Univ Rennes, CNRS, ISCR (Institut des Sciences Chimiques de Rennes) UMR 6226, F-35000 Rennes, France

Andres Saúl●

Aix Marseille Univ., CNRS, CINaM UMR 7325, Campus de Luminy Case 913, 13288 Marseille, France

We present a first-principles investigation of the magnetic and ferroelectric properties of BaCuF$_4$. Our calculations indicate that the magnetic topology is one-dimensional, with a Néel temperature smaller than 1 K, if existing. We also show that applying high-pressure values up to 40 GPa on BaCuF$_4$ does not induce three-dimensional magnetic order. In addition, our calculations predict that the polar phase is destabilized under pressure. The first consequence is to reduce the energy barrier between $Cmc2_1$ polar and $Cmcm$ nonpolar phases, enhancing the ability to reverse the polarization. The second consequence is the disappearance of ferroelectricity above a critical pressure of 12.6 GPa.

I. INTRODUCTION

The search for magnetoelectric materials, i.e., with coexisting magnetic and ferroelectric orders in the same phase [1,2], is a hot topic for both academic and technological reasons. It represents a playground to study new physics and chemistry arising from the interplay between spin, charge, orbital, and lattice degrees of freedom, and allows us to imagine devices in which magnetism is controlled by electric fields and vice versa, paving the way for many innovative applications in spintronics [3] and data storage [4]. However, we are still far from reaching the ideal multiferroic material, enabling a control of magnetism with a low-energy electric field at room temperature (RT) and with a high and switchable polarization. This technological bottleneck is directly related to the scarcity of multiferroics [5]. On the other hand, alternative routes have been proposed consisting of using epitaxial strain or high pressure to enhance or induce multiferroicity. Recently, it has been demonstrated that ferroelectricity can be induced by an epitaxial tensile strain in the ferromagnetic (FM) simple binary oxide EuO [6]. Similarly, we have demonstrated theoretically that under hydrostatic pressure, CuO may reach RT functioning with an increase of the polarization [7,8]. Kimura and coworkers have also shown that the orthorhombic phase of TbMnO$_3$ experiences a pressure-induced magnetoelectric phase transition leading to a giant spin-driven ferroelectric polarization [9].

In 2018, a promising compound has emerged not from the oxide family but the fluorides [10]. Based on first-principles calculations, BaCuF$_4$ was shown to exhibit weak ferromagnetism coupled to ferroelectricity. The work claimed the existence of an unusually high Néel temperature T_N of 275 K despite that magnetic susceptibility and electron paramagnetic resonance experiments on powder samples [11] evidenced a one-dimensional (1D) antiferromagnetic (AFM) behavior at high temperature and a FM contribution below 20 K that may be associated to the establishment of a three-dimensional (3D) order. A Néel temperature of about 275 K for a fluoride compound is surprising. First, BaCuF$_4$ belongs to a family of compounds BaMF$_4$ (with M = Mg, Mn, Fe, Co, Ni, Cu, and Zn), where the leading magnetic interactions of the other magnetic members (Mn, Fe, Co, Ni) are all AFM with long-range magnetic order appearing at lower temperatures, i.e., below 26.4, 54.2, 69.6, and 68.4 K for the Mn [12], Fe [13], Co [14], and Ni [15] compounds, respectively. Second, T_N = 275 K is far above the largest T_N value reported in the review article of Scott and Blinc on multiferroic fluorides [16], i.e., 148 K for KMnFeF$_6$.

These challenging results motivated us to study the magnetic properties of this compound in more detail and to explore the influence of high pressure on its properties. In this paper, we show from first-principles calculations and Monte Carlo simulations that BaCuF$_4$ is a pure 1D antiferromagnet, without any signature of 3D ordering (T_N smaller than 1 K). We also show that applying high-pressure values up to 40 GPa on BaCuF$_4$ does not induce 3D magnetic order. In addition, our calculations predict that the polar phase is destabilized under pressure and the ferroelectric polarization disappears above 12 GPa.

This paper is organized as follows. In Sec. II, we discuss the methods that we used for the calculation of the electronic, magnetic, and dynamical properties. In Secs. III and IV, we present and discuss the predicted properties at ambient pressure and under hydrostatic pressure, respectively.

II. CALCULATION METHODS

We performed density functional theory (DFT) calculations [17,18] using the VIENNA AB INITIO SIMULATION

*xavier.rocquefelte@univ-rennes1.fr

064421-1

PACKAGE [19] within the projector augmented plane wave (PAW) method [20–22]. We used the general-gradient approximation GGA-PBE parametrization [23,24] for the exchange-correlation potential and PAW potentials with the valence electronic configurations $5s^2 5p^6 6s^2$ for Ba, $3d^{10}4s^1$ for Cu, and $2s^2 2p^5$ for F. The localized d electrons of copper were treated using GGA+U [25,26] within the Dudarev formalism [27], with $U_{\mathrm{eff}} = 8$ eV. The basis set was defined using plane waves with a cutoff energy of 550 eV. A 24-atom cell ($Cmc2_1$ unit cell) has been used for the geometry optimizations and the calculations of relative energies and ferroelectric polarization, and a 96-atom cell ($2a$-b-$2c$ supercell) for the magnetic properties. The k-mesh was converged depending on the calculated property ($6 \times 2 \times 5$ and $6 \times 4 \times 5$ for geometry optimization and accurate calculations, respectively) [28]. A tolerance of 10^{-6} eV was applied during the electronic minimization, and the ion positions and lattice parameters were optimized until the magnitude of the forces on the ions was below 3.10^{-2} eV/Å.

The magnetic exchange interactions were estimated using the optimized atomic structures for each pressure (from 0 to 40 GPa) by mapping the computed magnetic spectra onto the energy spectra of a Heisenberg Hamiltonian,

$$\hat{H} = \hat{H}_0 + \sum_{i > j} J_{ij}\, \hat{S}_i \cdot \hat{S}_j, \tag{1}$$

where $\hat{H}_0$ is the Hamiltonian independent of spin, J_{ij} the magnetic coupling between the magnetic sites i and j, and $\hat{S}_i$ and $\hat{S}_j$ are the related quantum $S = 1/2$ spin operators. The broken-symmetry method [29,30] has been used to calculate the magnetic collinear coupling J_{ij} of the couple of magnetic sites ij [31–33]. The interaction between spins i and j can be evaluated from

$$J_{ij} = E(\uparrow_i \uparrow_j) + E(\downarrow_i \downarrow_j) - E(\uparrow_i \downarrow_j) - E(\downarrow_i \uparrow_j), \tag{2}$$

where $E(\sigma_i, \sigma_j)$ are the four spin configurations where the spins i and j take the values up or down while all the other spins are kept up. Hereafter, $J > 0$ indicates AFM coupling, and $J < 0$ indicates FM coupling.

To estimate the spontaneous polarization, we computed the Born effective charges (BEC) [34] defined as

$$Z_{ij}^* = \frac{\Omega}{e} \frac{\delta P_i}{\delta d_j}, \tag{3}$$

where Ω is the volume of the system, e the elementary charge, i and j are directions of the displacement of an ionic sublattice. Integrating this expression, one gets the spontaneous polarization defined as the difference of polarization ΔP between polar (ferroelectric) and nonpolar (paraelectric) phases,

$$P_s = \Delta P = \frac{e}{\Omega} \sum_i l_i \times \bar{Z}_i, \tag{4}$$

where l_i is the displacement of the ion i and $\bar{Z}_i$ the average Born effective charge between these two phases. In the case of BaCuF$_4$, the ferroelectric and paraelectric phases are $Cmc2_1$ and $Cmcm$, respectively (see below).

The Murnaghan equation of state, which gives pressure (P) as a function of volume (V), has been used to estimate the
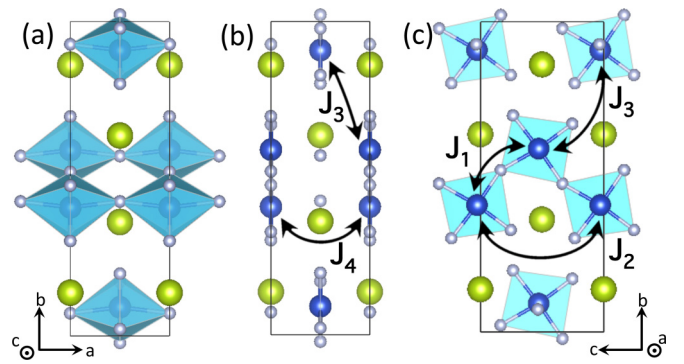

FIG. 1. Schematic representation of the $Cmc2_1$ ground-state atomic structure of BaCuF$_4$. It can be described alternatively as constituted of layers of corner-sharing distorted CuF$_6$ octahedra (a) or zigzag chains of corner-sharing CuF$_4$ square-planar environments (b, c). The magnetic exchange interactions are depicted. (All crystal visualization in this paper were performed using VESTA [39]).

critical pressure P_c at the phase transition [35],

$$P(V) = \frac{K_0}{K_0'} \left[\left(\frac{V}{V_0} \right)^{-K_0'} - 1 \right], \tag{5}$$

where V_0, K_0, and K_0' are the equilibrium volume, the modulus of compressibility, and its first derivative, respectively. Reversing Eq. (5) allows us to derive an expression for the enthalpy $H(P) = U + PV$ as a function of P. The critical pressure P_c is obtained when the difference of enthalpies between two phases $\Delta H(P)$ is zero.

Lattice-dynamics calculations have been performed with the PHONOPY package [36], via the supercell finite-displacement method [37]. A tolerance of 10^{-8} eV was applied during the electronic minimization, and the ion positions and lattice parameters were optimized until the magnitude of the forces on the ions was below 10^{-3} eV/Å. We found that a supercell of 216 atoms ($3 \times 1 \times 3$ expansion) with a gamma-centered $2 \times 2 \times 2$ k-point grid allows us to converge the shape of the phonon dispersion. From these data, an analysis of the dynamic stability of the polar and nonpolar phases has been realized by checking the presence of imaginary modes.

To estimate the Néel temperature and the evolution of the magnetic properties with temperature, we have performed Monte Carlo simulations implemented in the ALGORITHMS AND LIBRARIES FOR PHYSICS SIMULATIONS code [38]. We used the obtained J values from DFT calculations and a $S = \frac{1}{2}$ Heisenberg model. The simulations were performed with a cell containing 12 288 magnetic sites, 250 000 steps for the thermalization, and 1500 Monte Carlo steps per atom for the thermodynamic averages.

III. AMBIENT PRESSURE PROPERTIES

As mentioned above, BaCuF$_4$ belongs to a family of compounds BaMF$_4$ with M = Mg, Mn, Fe, Co, Ni, Cu, and Zn, which adopt a $Cmc2_1$ [11] structure and are all polar. As shown in Fig. 1 [39], BaCuF$_4$ can be described as layers of corner-sharing distorted CuF$_6$ octahedra, stacked along the **b** axis and separated from each other by Ba^{2+} ions.

Alternatively, the structure can be viewed as based on zigzag chains of edge-sharing CuF_4 square-planar environments, oriented along the **c** axis. The optimized a, b, and c cell parameters are 4.494, 14.208, and 5.661 Å, respectively, in good agreement with the experimental values (4.476, 13.972, and 5.551 Å) [11]. The Cu-F bond lengths in the equatorial plane are 1.6% larger on average than the experimental ones, i.e., 1.944 and 1.912 Å for relaxed and experimental mean distances, respectively. The longer apical Cu-F bond length is similar in the optimized and experimental structures (about 2.265 Å), confirming the distortion of the CuF_6 octahedra.

To investigate the magnetic properties of $BaCuF_4$, we have estimated the rotational invariant exchange interactions J_{ij} between spin sites i and j using the procedure described in Sec. II. As shown in Fig. 1, four different J_{ij} interactions can be defined, two intrachain (J_1 and J_2) and two interchain (J_3 and J_4). In the relaxed structure, the distance between the magnetic centers, i.e., Cu-Cu bond length, is 3.836, 5.661, 5.783, and 4.494 for J_1, J_2, J_3, and J_4, respectively. J_1 is also defined by a Cu-F-Cu superexchange angle of 154°. J_2 and J_3 can be described by their Cu-F-F-Cu dihedral angles of 0 and 164°, respectively. J_4 corresponds to a coupling involving the apical F atom, with a Cu-F-Cu angle of 166°. The present GGA+U estimation of the magnetic couplings leads to $J_1 = 222$ K, $J_2 = 7$ K, $J_3 = -2$ K, and $J_4 = 0$ K. It should be noted that $J_4 = 0$ K is expected although the Cu-Cu distance and the Cu-F-Cu angles are favorable for a sizable AFM interaction. Indeed, each Cu^{2+} ion has only one magnetically active $d_{x^2-y^2}$ orbital which is in the (b,c) plane. As a consequence, the magnetic exchange interaction related to J_4, which is along the a direction (perpendicular to the magnetically active orbitals), is zero. It is interesting to note that in $BaNiF_4$, where the Ni^{2+} ions are in a $3d^8$ electron configuration, the second magnetically active d_{z^2} orbital is responsible of a J_4 effective interaction which is indeed larger than J_1 [40,41]. Similar values were obtained in Ref. [10], i.e., $J_1 = 185$ K, $J_3 = -0.4$, and $J_4 = -0.5$ K (note that J_2 was not considered).

A rough estimate of J_1 can be obtained by comparing the experimental susceptibility, measured with a Faraday balance, to the magnetic susceptibility of a $S = 1/2$ AFM Heisenberg chain model [42] (see Fig. 2),

$$\chi_{cal}^{cgs} = \frac{10^6 \, g^2 \mu_B^2 N_A}{4\pi \, J_1} \, \frac{d_{eau} \, m_{material}}{d_{solid}^{material} \, m_{solution}} \, \chi^*, \qquad (6)$$

where χ^* is the calculated unitless susceptibility. The first part of the formula allows us to convert the unit in cgs, i.e., emu/Oe mol, with $g = 2.2$ the Landé factor, μ_B the Bohr magneton, and N_A the Avogadro number. The second part of the formula allows us to estimate the amount of magnetic particles in the solution, with d and m the densities and masses, respectively. The best fit is obtained for a mass percent of $BaCuF_4$ in solution of 8% and $J_1 = 267$ K, which is close to the GGA+U estimation of 222 K. In addition, the estimated Curie-Weiss temperature is 431 K, in close agreement with the experimental estimation of 430 K, confirming that the magnetic topology is strongly 1D with AFM interactions. The disagreement at low temperature between the model and the experimental susceptibilities is certainly due to paramagnetic impurities in the sample.
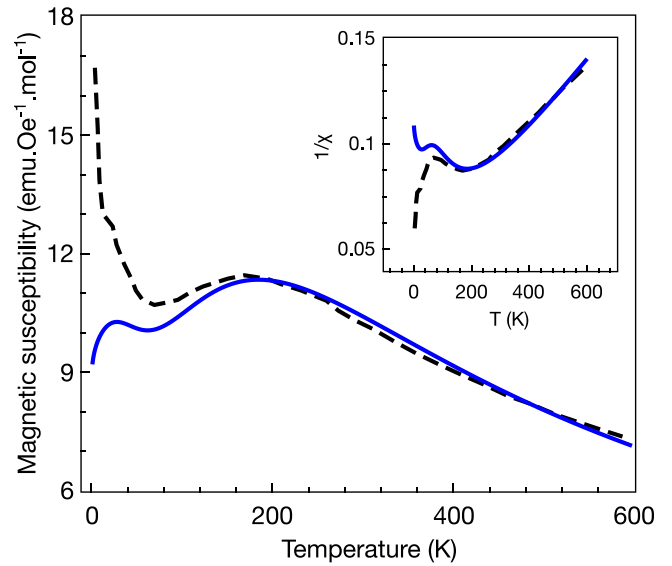

FIG. 2. The experimental (black dashed curve) magnetic susceptibility [11] is compared to a calculated one (blue solid curve) based on an $S = 1/2$ antiferromagnetic Heisenberg uniform chain model with $J = 267$ K [42]. The inset shows the corresponding inverse magnetic susceptibilities as a function of the temperature.

Last but not least, we have used the semiempirical random phase approximation expression, developed by Yasuda *et al.* [43], for the estimation of T_N for a quasi-1D AFM Heisenberg cubic lattice,

$$J' = \frac{T_N}{4c\sqrt{\ln\left(\frac{\lambda J}{T_N}\right) + \frac{1}{2}\ln\left(\ln\left(\frac{\lambda J}{T_N}\right)\right)}}, \qquad (7)$$

where J and J' represent, respectively, the intra- and interchain magnetic couplings. J and J were defined by comparing the energy expressions of the ground-state magnetic order of $BaCuF_4$ ($E = J_1 - J_2 + 2J_3$) and of a quasi-1D AFM Heisenberg cubic lattice ($E = J + 2J$). It leads to $J = J_1 - J_2$ and $J' = J_3$. For c and λ parameters, we have used the values proposed in Yasuda *et al.* [43], i.e., $c = 0.233$ and $\lambda = 2.6$. Using the J_{ij} values previously calculated in GGA+U, it leads to T_N smaller than 1 K, far from the reported value of 275 K. Using these parameters, Kurzydłowski and Grochala systematically obtained larger T_N values than the experimental ones for quasi-1D spin-half copper fluoride antiferromagnets [44]. We thus expect an overestimated T_N value using Eq. (7).

In addition, we simulated the fourth-order Binder cumulant U_L [45–47] defined as

$$U_L(T) = 1 - \frac{<m^4>}{3<m^2>^2} \qquad (8)$$

for a system of size L, where m is the magnetization of the system. When the value of $U_L(T)$ becomes different of zero for $T = T_c$, then we obtain the critical temperature T_c if L is large enough to approach the thermodynamic limit. However, no sign of a critical temperature in the range going from 1 to 300 K was found. All these results confirm the 1D character of the magnetic interactions in $BaCuF_4$ with no proof of the establishment of 3D magnetic order.
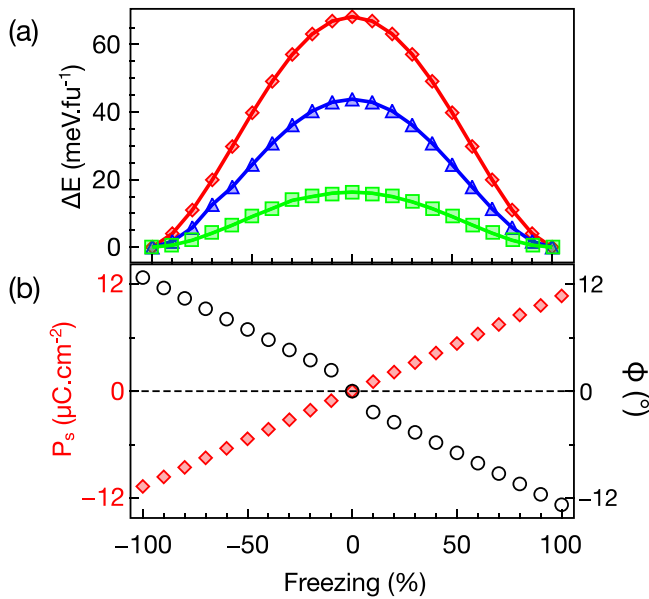
FIG. 3. (a) Double-well energy profile obtained by ferroelectric switching between positive and negative spontaneous polarization along the **c** axis for 0, 4 and 8 GPa, represented by red diamonds, blue triangles, and green squares, respectively. (b) Spontaneous polarization reversal going from -10.7 to $+10.7$ $\mu C.cm^{-2}$ at 0 GPa, and octahedral rotation angle Φ, where a full octahedral reversal is observed.

Concerning the ferroelectric properties at ambient pressure, we have estimated the spontaneous polarization of $BaCuF_4$ using Eq. (4). The positions of the ions on the path between the two phases were obtained using tools of the Bilbao crystallographic server. PSEUDO [48] was used to generate the *Cmcm* structure from the relaxed *Cmc2₁* structure and AMPLIMODES [49,50] to create the pathway between the two phases, which consists of a rotation of the CuF_6 octahedra, without any noticeable displacement of Cu and Ba atoms. This structural distortion can be associated to the instability evidenced by the imaginary modes in the phonon dispersion of the *Cmcm* phase (see below).

Figure 3(a) shows the energy well (energy difference between *Cmc2₁* and *Cmcm* phases) at ambient pressure and for $P = 4$ and 8 GPa. The related polarization, as a function of the ferroelectric distortion, is also shown for $P = 0$ GPa [Fig. 3(b)]. Freezing values of -100, 0, and 100% correspond to octahedral rotation angles (Φ) of $+12.7$, 0, and $-12.7°$ (black open circles), and spontaneous polarization (P_s) of -10.7, 0, $+10.7$ $\mu C.cm^{-2}$ (red diamonds), respectively. Such computed P_s values are very close to the ones obtained in Ref. [10]. At ambient pressure, $\Delta E = 68$ meV/f.u., which is in the range of the value calculated for $BaCoF_4$ ($\Delta E = 58$ meV/f.u. [40]), for which ferroelectric switching has been experimentally demonstrated [51]. It should be noted that ΔE is twice larger than in Ref. [10]. To understand the possible origin of this difference, we have tested the impact of changing the functional and the U_{eff} value. It shows that ΔE is reduced to 40 and 32 meV/f.u. when using PBE+U ($U_{eff} = 4$ eV) and PBEsol+U ($U_{eff} = 8$ eV), respectively. It confirms that the ΔE value strongly depends on the functional and the U_{eff} value.
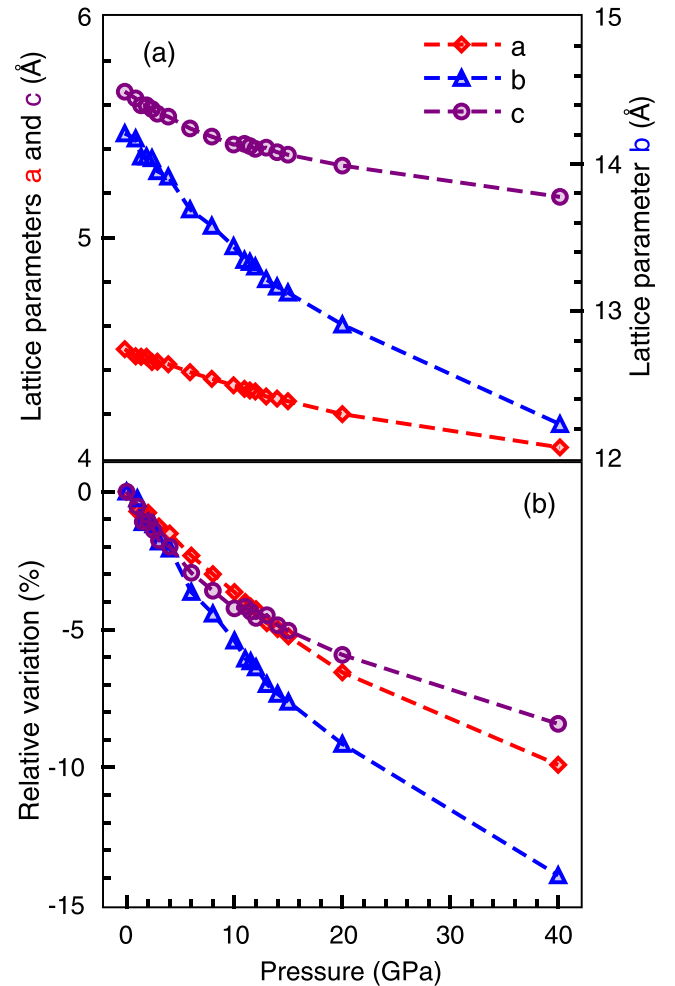

FIG. 4. (a) Calculated cell parameters of $BaCuF_4$ and (b) their relative variations under high pressure.

IV. EFFECT OF HYDROSTATIC PRESSURE

We will now consider the influence of applying hydrostatic pressure on this compound. Figure 4 shows the evolution of the cell parameters under pressure, from 0 to 40 GPa. Our calculations evidence that the softest direction, i.e., with the largest relative compressibility, is the **b** axis, by a factor of 2 compared to **a** and **c** axes. From 0 to 12 GPa, the relative variation of the two hardest directions, **a** and **c**, are nearly the same, and for $P > 12$ GPa, **a** direction becomes smoother than **c** direction. Such an ordering directly reflects the strength of the interactions which are stronger along **c**, i.e., the direction of the chains, than along **a** and **b**, which, respectively, correspond to the directions of the longer Cu-F bonds (Jahn-Teller distortion) and the stacking of the layers. The change of slope computed at about 12 GPa appears to be the signature of a structural transition from *Cmc2₁* to *Cmcm* phases.

To have a better estimate of the critical pressure (P_c), at which the nonpolar *Cmcm* phase becomes more stable than the polar *Cmc2₁* one, the Murnaghan equation of state Eq. (5) has been used. Figure 5 shows the evolution of the total energy of each phase as a function of the cell volume under an applied hydrostatic pressure. The inset of Fig. 5 gives the enthalpy difference $\Delta H = H_{Cmc2_1} - H_{Cmcm}$ as a function of
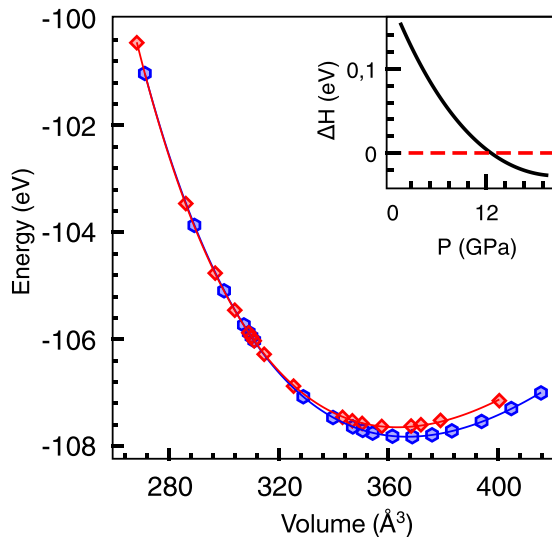
FIG. 5. Energies of the polar ($Cmc2_1$) in blue hexagon, and nonpolar ($Cmcm$) in red diamond, phases versus volume. The inset shows the calculated difference of enthalpies between the polar and nonpolar phases : $\Delta H = H_{Cmc2_1} - H_{Cmcm}$. A critical pressure appears at 12.64 GPa where the centrosymmetric phase becomes more stable than the polar phase.

the applied pressure P. It allows to estimate a critical pressure $P_c = 12.64$ GPa.

Figure 6 shows the calculated phonon dispersions of the $Cmcm$ nonpolar phase for $P = 0$ and 8 GPa. While the com-
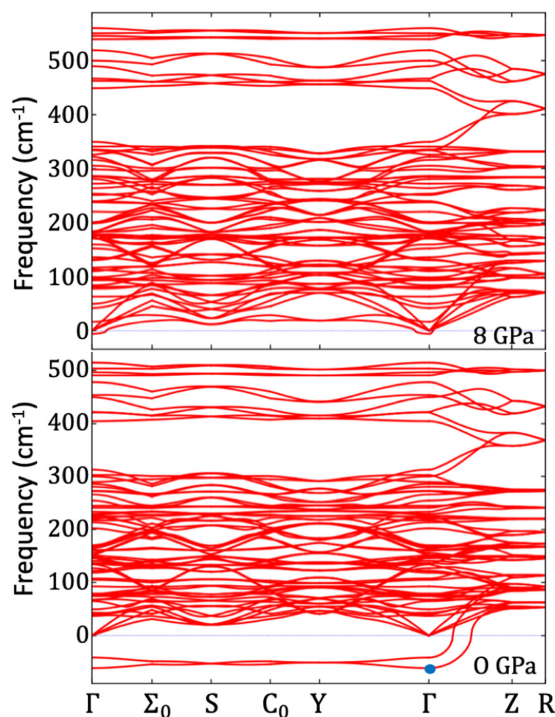

FIG. 6. Phonon dispersion curves of BaCuF$_4$ for phase $Cmcm$ at 0 GPa (lower panel) and at 8 GPa (upper panel). Negative branches (i.e., imaginary and thus unstable modes) are observed and disappear under pressure. The Γ_2^- instability mode is highlighted by a blue dot.
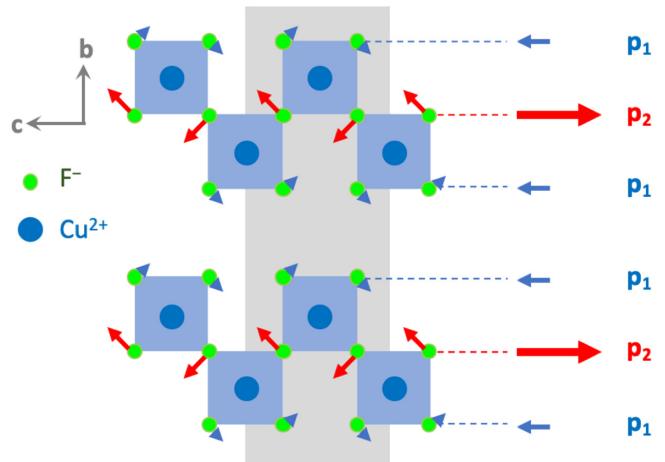

FIG. 7. Sketch of the largest atomic displacements associated to the Γ_2^- instability mode. The arrows on the right side represent the electric dipoles generated by the displacement of F$^-$ ions. One slab is composed of three layers of F$^-$ ions stacked along the **b** axis. p_1 and p_2 dipoles arise from outer and inner layers, respectively. The crystallographic unit cell is represented by a grey rectangle. Ba atoms are not shown for simplicity.

puted phonon dispersions of the $Cmc2_1$ at 0 and 8 GPa do not show any imaginary modes (Fig. S1 in the Supplemental Material [52]), imaginary modes can be noticed along the way $\Gamma - \Sigma_0 - S - C_0 - Y - \Gamma$ at ambient pressure in the high-symmetry $Cmcm$ phase. It confirms its dynamical instability and evidences soft modes involving the cooperative rotation of the CuF$_6$ octahedra, leading to a transition toward the $Cmc2_1$ polar phase, which is the structural ground state from 0 to $P_c = 12.64$ GPa. In particular, when looking at the high-symmetry points, we found the following unstable modes: Γ_2^- at 62, S_2^+ at 53, and Y_2^- at 51 icm^{-1}, very close to the reported values [10]. These imaginary modes progressively disappear under pressure. As shown for $P = 8$ GPa, a small residue remains at the Γ point, and no more unstable modes are found at both S and Y points. The Γ_2^- mode is polar and is mainly based on the displacements of the F$^-$ ions, as depicted in Fig. 7. It involves a ferrodistortive rotation of the CuF$_6$ octahedra around the **a** axis. The interpretation of the role of the Γ_2^- mode in the emergence of ferroelectricity can be understood using similar arguments as the ones used for the layered perovskite La$_2$Ti$_2$O$_7$ [53]. The crystallographic unit cell can be viewed as based on two [Ba$_2$Cu$_2$F$_8$] **b**-orientated slabs, each one containing two outer layers and one inner layer of fluorine atoms, respectively, labeled F$_1$ and F$_2$. The displacement of F$^-$ ions in each **b**-orientated layer gives rise to an electric dipole along the **c** direction, i.e., p_1 and p_2 dipoles, for F$_1$ and F$_2$ layers, respectively. The total dipole of a slab is then $p_{\text{slab}} = 2p_1 + p_2$. Since no symmetry constraint exists between F$_1$ and F$_2$, the dipole of a slab will be nonzero. In addition, the amplitude of the movement is more than twice larger for F$_2$ than F$_1$ atoms. Finally, in the Γ_2^- mode, the two slabs of the unit cell exhibit identical collective displacements, giving rise to a net macroscopic polarization $P_s = 2p_{\text{slab}}$.

A deeper analysis of the structural evolution under pressure can be realized considering the variation of geometrical parameters (bond length and angle) between the magnetic sites.
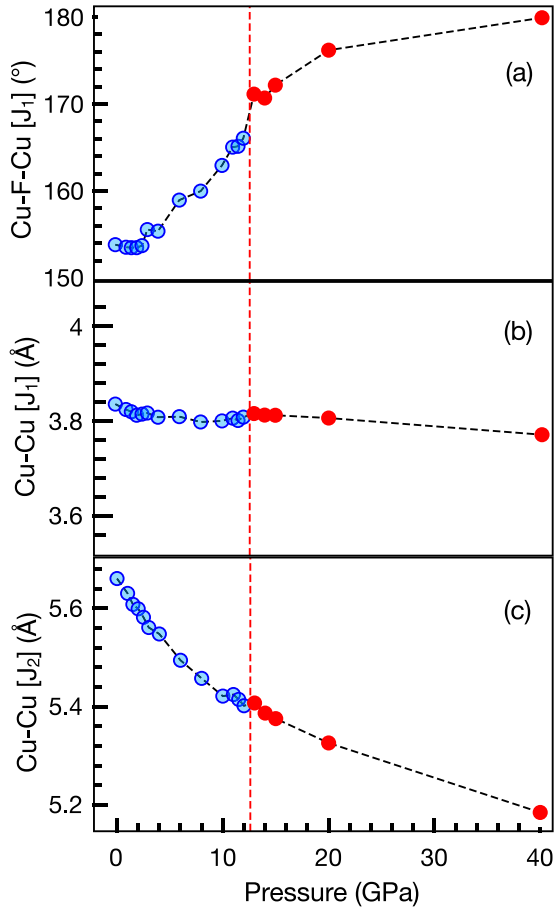
FIG. 8. Dependence of the structural parameters with applied pressure. (a) Superexchange angle (Cu-F-Cu) and (b) Cu-Cu distance associated to the effective exchange interaction J_1. (c) Cu-Cu distance associated to the supersuperexchange interaction J_2. The effect of the pressure is more important on the superexchange angle and the Cu-Cu distance associated to supersuperexchange. The critical pressure corresponding to the phase transition from $Cmc2_1$ to $Cmcm$ phases is depicted by a red dashed line. The points below (above) P_c are represented in blue (red).

The evolution under pressure of the Cu-F-Cu angle and the Cu-Cu distance related to the largest coupling (J_1) is shown in Figs. 8(a) and 8(b). While the Cu-Cu distance slightly decreases under pressure (from 3.84 to 3.77 Å), the Cu-F-Cu angle strongly increases (from 154 to 180°). Such an opening of the superexchange angle explains the increase of J_1 under pressure as illustrated in Fig. 9(a), which goes from 222 to 562 K, when P increases from 0 to 40 GPa. Figure 8(c) provides the variation under pressure of the Cu-Cu distance related to J_2. The Cu-Cu distance strongly decreases under pressure (from 5.7 to 5.2 Å), explaining the large increase of J_2 from 7 to 76 K, when P increases from 0 to 40 GPa. The two other couplings (J_3 and J_4) do not change significantly under pressure.

Using the so-obtained J values, we performed Monte Carlo simulations to estimate the dependence of the magnetic susceptibility with temperature [Fig. 9(b)]:

$$\chi = \frac{\partial M}{\partial H}\bigg|_{H=0} \propto \frac{<M^2> - <|M|>^2}{k_b T}. \qquad (9)$$
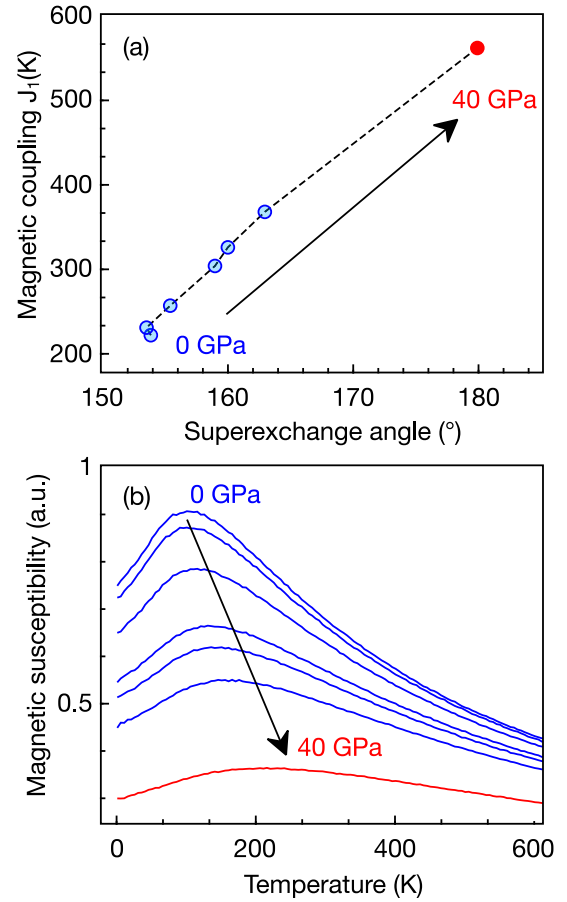

FIG. 9. (a) Dependence of the effective exchange interaction J_1 with the Cu-F-Cu superexchange angle. (b) Monte Carlo simulations of the temperature dependence of the magnetic susceptibility for different values of hydrostatic pressure ($P = 0, 2, 4, 6, 8, 10, 40$ GPa). The gradual pressure increase is highlighted by an arrow in both panels.

All the magnetic susceptibility curves have the same feature, which is characteristic of low-dimensional magnets. The maximum of the magnetic susceptibility is shifted toward higher temperatures under pressure, as expected from the increase of the J_1 value.

Finally, we have estimated the impact of the hydrostatic pressure on the ferroelectric properties. As expected, the energy barrier decreases with pressure with values of 68, 44, and 16 meV/f.u., respectively, for $P = 0, 4$ and 8 GPa [Fig. 3(a)]. Such results evidence that (i) for $P < P_c$ the ferroelectric switching is easier under pressure and (ii) for $P > P_c$ the ferroelectricity vanishes. Indeed, Fig. 10(a) shows the computed polarization (P_s) in the ground state, which slightly increases from 0 to 2 GPa, reaching a value of $11 \mu C.cm^{-2}$ and then decreases from 2 GPa to 11.5 GPa, reducing P_s by a factor of 2. At about 12.6 GPa, the polar phase becomes unstable, leading to a phase transition toward the nonpolar $Cmcm$ phase, and $P_s = 0$.

Figure 10(b) shows GGA+U calculations including spin orbit to study the magneto-electric coupling in this system. Our calculations, at zero pressure, show a preference of the magnetic moments to lay along the **b** direction, with a small
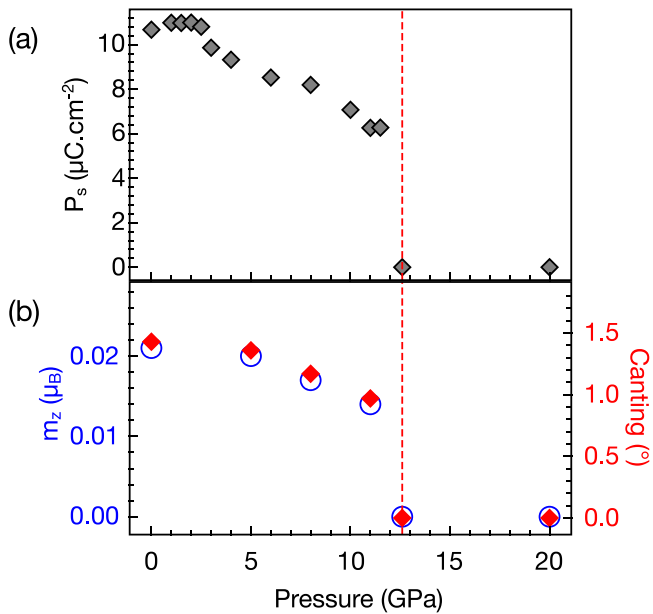
FIG. 10. (a) Pressure dependence of the spontaneous polarization calculated from the Born effective charges. At 12.6 GPa, a phase transition occurs from $Cmc2_1$ to $Cmcm$, leading to the disappearance of ferroelectricity. (b) Pressure dependence of the magnetic moment along the c axis (left axis) and the corresponding canting angle (right axis) obtained from the spin-orbit magnetic calculations (see text). The critical pressure is depicted by a red dashed line.

canting along the c axis (magnetic moment components of $m_x = 0$, $m_y = 0.844$, and $m_z = 0.021$ μ_B/Cu). Such results agree with the ones of Garcia-Castro *et al.* [10]. It should be noted that similar results were reported by Ederer and Spaldin [40] and Lévêque *et al.* [41] for BaNiF$_4$, which is a $S = 1$ system with Ni^{2+} ions in a $3d^8$ electronic configuration. Interestingly, in BaNiF$_4$, the supplementary magnetic

orbital is responsible for the apparition of an additional AFM interaction along the a direction (J_4 in Fig. 1), leading to a 2D magnetic topology. Moreover, the single ion anisotropy permits the establishment of long-range magnetic order at finite temperature, as observed experimentally below 70 K [54]. In contrast, BaCuF$_4$ is essentially a 1D system where the anisotropy allows Ising-like AFM magnetic order at zero temperature with the magnetic moments oriented along the b axis. The small tilt associated with the canting is a consequence of the distortion of the $Cmc2_1$ polar phase and produces weak FM order along the c axis [10,40,41]. Interestingly, m_z decreases with pressure and vanishes at $P = P_c$ [see Fig. 10(b)], confirming the strong coupling between the weak-FM order and the electric polarization in BaCuF$_4$.

In conclusion, we have reconsidered the feasibility of multiferroicity close to RT in BaCuF$_4$ using first-principles calculations. The magnetic exchange interactions in BaCuF$_4$ evidence a 1D-topology, with a T_N value smaller than 1 K, if existing. Applying high-pressure reduces the energy barrier between polar and nonpolar phases, enhancing the ability to reverse the ferroelectric polarization. Above 12.6 GPa, the polar phase becomes unstable and a phase transition toward the nonpolar phase takes place with the loss of the ferroelectric polarization. It should be interesting to extend such an investigation to the other members of the family BaMF$_4$, where M is a transition metal (Fe, Mn, Cu, Ni, Zn, Mg).

[1] J. Young, A. Stroppa, S. Picozzi, and J. M. Rondinelli, J. Phys.: Condens. Matter **27**, 283202 (2015).

[2] N. A. Benedek and C. J. Fennie, Phys. Rev. Lett. **106**, 107204 (2011).

[3] M. Fiebig, T. Lottermoser, D. Meier, and M. Trassin, Nat. Rev. Mater. **1**, 16046 (2016).

[4] A. Roy, R. Gupta, and A. Garg, Adv. Condens. Matter Phys. **2012**, 926290 (2012).

[5] N. Hill, J. Phys. Chem. B **104**, 6694 (2000).

[6] N. J. C. Ingle and I. S. Elfimov, Phys. Rev. B **77**, 121202(R) (2008).

[7] X. Rocquefelte, K. Schwarz, P. Blaha, S. Kumar, and J. Van Den Brink, Nat. Commun. **4**, 2511 (2013).

[8] W. Lafargue-Dit-Hauret, D. Braithwaite, A. D. Huxley, T. Kimura, A. Saúl, and X. Rocquefelte, Phys. Rev. B **103**, 214432 (2021).

[9] T. Aoyama, K. Yamauchi, A. Iyama, S. Picozzi, K. Shimizu, and T. Kimura, Nat. Commun. **5**, 4927 (2014).

[10] A. C. Garcia-Castro, W. Ibarra-Hernandez, E. Bousquet, and A. H. Romero, Phys. Rev. Lett. **121**, 117601 (2018).

[11] J.-M. Dance, Mater. Res. Bull. **16**, 599 (1981).

[12] J. F. Scott, Rep. Prog. Phys. **42**, 1055 (1979).

[13] P.-Y. Arquès, L. Holmes, H. J. Guggenheim, and D. E. Cox, J. Phys. France **32**, 1 (1971).

[14] M. Eibschütz, L. Holmes, H. J. Guggenheim, and D. E. Cox, Phys. Rev. B **6**, 2677 (1972).

[15] W. Kleemann, F. J. Schafer, and J. Nouet, J. Phys. C **14**, 4447 (1981).

[16] J. F. Scott and R. Blinc, J. Phys.: Condens. Matter **23**, 113202 (2011).

[17] P. Hohenberg and W. Kohn, Phys. Rev. **136**, B864 (1964).

[18] W. Kohn and L. J. Sham, Phys. Rev. **140**, A1133 (1965).

[19] G. Kresse and J. Furthmüller, Phys. Rev. B **54**, 11169 (1996).

[20] P. E. Blöchl, Phys. Rev. B **50**, 17953 (1994).

[21] G. Kresse and D. Joubert, Phys. Rev. B **59**, 1758 (1999).

[22] D. Hobbs, G. Kresse, and J. Hafner, Phys. Rev. B **62**, 11556 (2000).

[23] J. P. Perdew, K. Burke, and M. Ernzerhof, Phys. Rev. Lett. **77**, 3865 (1996).

[24] J. P. Perdew, A. Ruzsinszky, G. I. Csonka, O. A. Vydrov, G. E. Scuseria, L. A. Constantin, X. Zhou, and K. Burke, Phys. Rev. Lett. **100**, 136406 (2008).

[25] J. Hubbard, Proc. Roy. Soc. London A **276**, 238 (1963).

[26] A. I. Liechtenstein, V. I. Anisimov, and J. Zaanen, Phys. Rev. B **52**, R5467 (1995).

[27] S. L. Dudarev, G. A. Botton, S. Y. Savrasov, C. J. Humphreys, and A. P. Sutton, Phys. Rev. B **57**, 1505 (1998).

[28] H. J. Monkhorst and J. D. Pack, Phys. Rev. B **13**, 5188 (1976).

[29] C. van Wüllen, J. Phys. Chem. A **113**, 11535 (2009).

[30] H. Xiang, C. Lee, H.-J. Koo, X. Gong, and M.-H. Whangbo, Dalton Trans. **42**, 823 (2013).

[31] A. Saúl and G. Radtke, Phys. Rev. Lett. **106**, 177203 (2011).

[32] D. Vaclavkova, A. Delhomme, C. Faugeras, M. Potemski, A. Bogucki, J. Suffczyński, P. Kossacki, A. R. Wildes, B. Grémaud, and A. Saúl, 2D Mater. **7**, 035030 (2020).

[33] A. Saúl, N. Gauthier, R. M. Askari, M. Ct, T. Maris, C. Reber, A. Lannes, D. Luneau, M. Nicklas, J. M. Law *et al.*, Phys. Rev. B **97**, 064414 (2018).

[34] N. A. Spaldin, J. Solid State Chem. **195**, 2 (2012), Polar Inorganic Materials: Design Strategies and Functional Properties.

[35] F. D. Murnaghan, Proc. Natl. Acad. Sci. USA **30**, 244 (1944).

[36] A. Togo and I. Tanaka, Scr. Mater. **108**, 1 (2015).

[37] L. Chaput, A. Togo, I. Tanaka, and G. Hug, Phys. Rev. B **84**, 094302 (2011).

[38] B. Bauer, L. D. Carr, H. G. Evertz, A. Feiguin, J. Freire, S. Fuchs, L. Gamper, J. Gukelberger, E. Gull, S. Guertler, A. Hehn, R. Igarashi, S. V. Isakov, D. Koop, P. N. Ma, P. Mates, H. Matsuo, O. Parcollet, G. Pawłowski, J. D. Picon *et al.*, J. Stat. Mech.: Theory Exp. (2011) P05001.

[39] K. Momma and F. Izumi, J. Appl. Crystallogr. **41**, 653 (2008).

[40] C. Ederer and N. A. Spaldin, Phys. Rev. B **74**, 024102 (2006).

[41] J. Lévêque, E. Rebolini, A. Saúl, and M.-B. Lepetit, Eur. Phys. J. B **94**, 214 (2021).

[42] D. C. Johnston, R. K. Kremer, M. Troyer, X. Wang, A. Klümper, S. L. Bud'ko, A. F. Panchula, and P. C. Canfield, Phys. Rev. B **61**, 9558 (2000).

[43] C. Yasuda, S. Todo, K. Hukushima, F. Alet, M. Keller, M. Troyer, and H. Takayama, Phys. Rev. Lett. **94**, 217201 (2005).

[44] D. Kurzydłowski and W. Grochala, Phys. Rev. B **96**, 155140 (2017).

[45] K. Binder and D. Heermann, *Monte Carlo Methods in Statistical Physics* (Springer, Berlin, Heidelberg, 1979)

[46] K. Binder, Z. Phys. B **43**, 119 (1981).

[47] K. Binder, Phys. Rev. Lett. **47**, 693 (1981).

[48] C. Capillas, E. S. Tasci, G. de la Flor, D. Orobengoa, J. M. Perez-Mato, and M. I. Aroyo, **226**, 186 (2011)

[49] D. Orobengoa, C. Capillas, and J. Perez-Mato, J. Appl. Crystallogr. **42**, 820 (2009).

[50] J. Perez-Mato and D. Orobengoa, Acta Crystallogr., Sect. A: Found. Crystallogr. **66**, 558 (2010).

[51] M. Eibschütz Jr., H. Guggenheim, S. Wemple, I. Camlibel, and M. DiDomenico, Phys. Lett. A **29**, 409 (1969).

[52] See Supplemental Material at http://link.aps.org/supplemental/10.1103/PhysRevB.106.064421 for details concerning the phonon calculations.

[53] J. López-Pérez and J. Íñiguez, Phys. Rev. B **84**, 075121 (2011).

[54] D. E. Cox, M. Eibschütz, H. J. Guggenheim, and L. Holmes, J. Appl. Phys. **41**, 943 (1970).